frontiers | Frontiers in Immunology

Prediction model of axillary lymph node status using an automated breast volume ultrasound radiomics nomogram in early breast cancer with negative axillary ultrasound

Qianqing Ma[1,2†], Junli Wang[3†], Zhengzheng Tu[4†], Jingwen She[5], Jianhui Zhu[3], Feng Jiang[1]* and Chaoxue Zhang[2]*

[1]Department of Ultrasound, The First Affiliated Hospital of Wannan Medical College, Wuhu, China, [2]Department of Ultrasound, The First Affiliated Hospital of Anhui Medical University, Hefei, China, [3]Department of Ultrasound, The Second People's Hospital of Wuhu, Wuhu, China, [4]Anhui Provincial Key Laboratory of Multimodal Cognitive Computation, School of Computer Science and Technology, Anhui University, Hefei, China, [5]Department of Ultrasound, West China Second Hospital, Sichuan University, Chengdu, China

Background: Construction and validation of an automated breast volume ultrasound (ABVS)-based nomogram for assessing axillary lymph node (ALNs) metastasis in axillary ultrasound (AUS)-negative early breast cancer.

Methods: A retrospective study of 174 patients with AUS-negative early-stage breast cancer was divided into a training and test with a ratio of 7:3. Radiomics features were extracted by combining images of intra-tumor and peri-tumor ABVS. Select the best classifier from 3 machine learning techniques to build Model 1and radiomics-score (RS). Differences in ER, PR, Her-2, Ki-67 expression were analyzed for intra-tumoral and peri-tumoral habitat radiomics features. Model 2 (based on sonogram features) and Model 3 (based on RS and sonogram features) were constructed by multivariate logistic regression. Efficiency of the models was evaluated by the area under the curve (AUC). Plotting the nomogram and evaluating its treatment in ALN≥3 according to Model 2 and Model 3.

Result: Intratumoral and peritumoral 5 mm radiomics features were screened using least absolute shrinkage and selection operator (LASSO), and logistic regression was used as a classifier to build the best-performing Model 1. Using unsupervised cluster analysis, intratumoral and peritumoral 5mm were classified into 3 habitats, and they differed in PR and Her-2 expression. Model 2 (combining diameter and microcalcification) and Model 3 (combining RS and microcalcification) were created by multivariate logistic regression. Model 3 achieves the highest AUC in both the training (0.827) and validation (0.768) sets. The Nomo-score was calculated based on nomogram-model2 and

nomogram-model3, revealing a positive correlation between ALN burden and Nomo-score. Combined with the optimal thresholds, nomogram-model2 screened 54.6%-100% of patients with ALN $\geq$3 and nomogram-model3 screened 81.8%-100% of patients with ALN $\geq$3.

Conclusion: The ABVS-based nomogram is an effective tool for assessing ALN metastasis, and it can provide a preoperative basis for individualized treatment of breast cancer.

Introduction

Axillary lymph node (ALN) status is the most strongly associated factor affecting the survival and prognosis of breast cancer patients (1, 2). Although sentinel lymph node (SLN) biopsy is widely used to detect ALN status. However, the false-negative rate of SLNB is 5.5%-16.7% (3, 4), and SLNB may be associated with sensory nerve damage, lymphedema, and limited shoulder motion (5). In addition, according to the ACOSOG Z0011 trial, patients with SLN metastases of less than 2 early-stage breast cancers who do not undergo axillary surgery do not have affected overall survival and disease-free survival rates (6, 7). Therefore, ALN status is adequately assessed by radiographic methods prior to surgery to minimize unnecessary invasive exploration.

The most valuable radiological method for assessing ALNs is axillary ultrasound (AUS) (8–10). Owing to the noninvasive and inexpensive nature of ultrasound, it is very suitable for long-term observation of ALNs. Approximately 15.5-35.0% of AUS negatives show positivity on pathology, which makes it particularly important to reduce false negatives (11–13). Studies have shown that adding tumor characteristics to the diagnosis of ALNs can significantly reduce this deficiency of AUS (13). Certain ultrasound features of primary breast cancer are associated with ALN metastasis, such as the diameter of the lesion, microcalcification, architectural distortion, and tumor distance from the skin (13–18).

Furthermore, with the advancement of pattern recognition tools, radiomics has attracted increasing interest. Combining the imaging features of a lesion with radiomics features has greatly improved diagnostic performance (17, 19, 20). Radiomics is the process of converting medical images into mineable data by extracting high-throughput quantitative features that effectively reduce inter-examiner variability. In the past, free-form imaging methods and the reliance on adjustable parameters during the examination made the development of radiomics in ultrasound difficult (21), and the emergence of an automatic breast volume scanner (ABVS) has solved this problem. ABVS allows comprehensive and standardized scanning of the entire breast and coronal and sagittal display in specific workstations. The coronal plane of the lesion provides additional information for diagnosis (22), and standardized images also open up new opportunities for ultrasound radiomics (23).

Therefore, we aimed to develop and validate two nomograms (one based on sonogram features and the other based on radiomics and sonogram features) for assessing ALN status in AUS-negative early-stage breast cancers and to explore the value of the nomogram for the preoperative assessment of patients with ALN $\geq$3.

Materials and methods

Patient

The study was approved by the Institutional Review Board and requirement for informed consent was waived (PJ2023-07-11).

A retrospective collection of 499 patients who were diagnosed with breast cancer by histopathology between November 2017 and August 2021 and underwent ABVS at our institution was performed. The inclusion criteria were as follows: (1) patients who underwent SLNB or ALND; (2) unifocal masses ≤ 5 cm in diameter (T1 and T2 stages); (3) ABVS within 2 weeks prior to SLNB or ALND; and (4) no suspicious lymph nodes on AUS (asymmetric or diffuse thickening of the lymph node cortex, an LN with a cortex thickness ≥ 3 mm loss of hilum, and nonhilar blood flow) (24). The exclusion criteria were as follows: (1) patients who received chemotherapy, radiotherapy or endocrine therapy, (2) patients with multifocal or bilateral breast cancer, and (3) patients with nonoccupying lesions without demarcated borders (Appendix Figure 1). 174 patients were finally included in this study and randomized into training and test sets at a ratio of 7:3.

Baseline clinical data were acquired from the patient medical record system, including age, pathologic type, immunohistochemical (IHC) results and postoperative ALN status (ALN+ or ALN-). ALN+ patients were further classified into low burden (1-2 ALNs) and high burden (≥3 ALNs) groups. IHC was performed to assess HER-2, Progesterone Receptor (PR), Estrogen Receptor (ER) and Ki-67 status and recorded as positive (+) or negative (-).

Image acquisition and assessment

Details of image acquisition are provided in Appendix A.1. Reader 1 and Reader 2 (11 and 20 years of experience, respectively) analyzed these images. Cases of disagreement were independently resolved by a third Reader (Reader 3, 25 years of experience). None of the sonographers had knowledge of the pathological results. Orientation (parallel or not parallel), margin (circumscribed, noncircumscribed), shape (regular or irregular), echogenicity (hypoechoic, hybrid echo or extremely low echo), microcalcification, tumor location (left, right), quadrant (upper inner, lower inner, upper outer, lower outer, central), convergence sign, distance from nipple, and distance from skin and maximum diameter of the lesion were recorded.

Segmentation and extraction of radiomics features

The flowchart of the study was showed in Figure 1. Tumor regions of interest (ROIs) were manually depicted slice-by-slice by Reader 1 using ITK-SNAP 3.6. Next, using Python 3.7, areas 1, 3, 5, 7, and 9 mm around the ROI will be generated. Figure 2 shows an example of the ROI segmentation and expansion process for ABVS. Fifty images were randomly selected and re-segmented by Reader 1 and Reader 2 after 2 weeks to calculate intra- and inter-class correlation coefficients (ICC). Radiomics features were extracted using the "PyRadiomics (3.7.0)" Python package (Detailed in Appendix A.2).

Feature screening, machine learning classifier, and Model 1 building

The obtained intratumoral region (ITR) features are preprocessed and the model is constructed using classifiers employing logistic regression (LR), random forest (RF) and support vector machine (SVM). An optimal ML classifier was used to construct a joint ITR and peritumoral region (PTR) radiomics model, named Model 1. The radiomics-score (RS) was
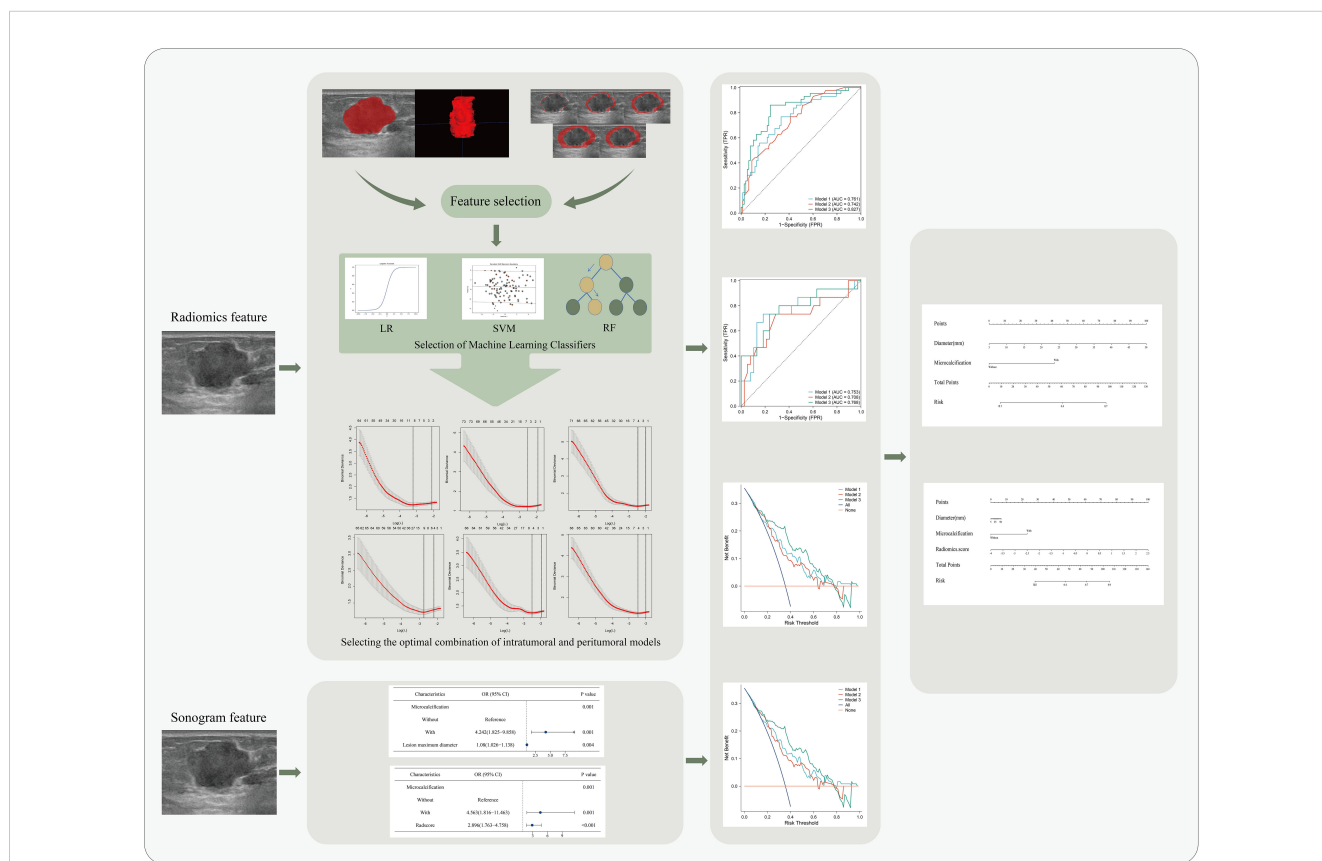

FIGURE 1
Flowchart of a nomogram for predicting lymph node metastasis in breast cancer.LR, logistic regression; SVM, support vector machine; RF, random forest; OR, odds ratio; CI, confidence interval.
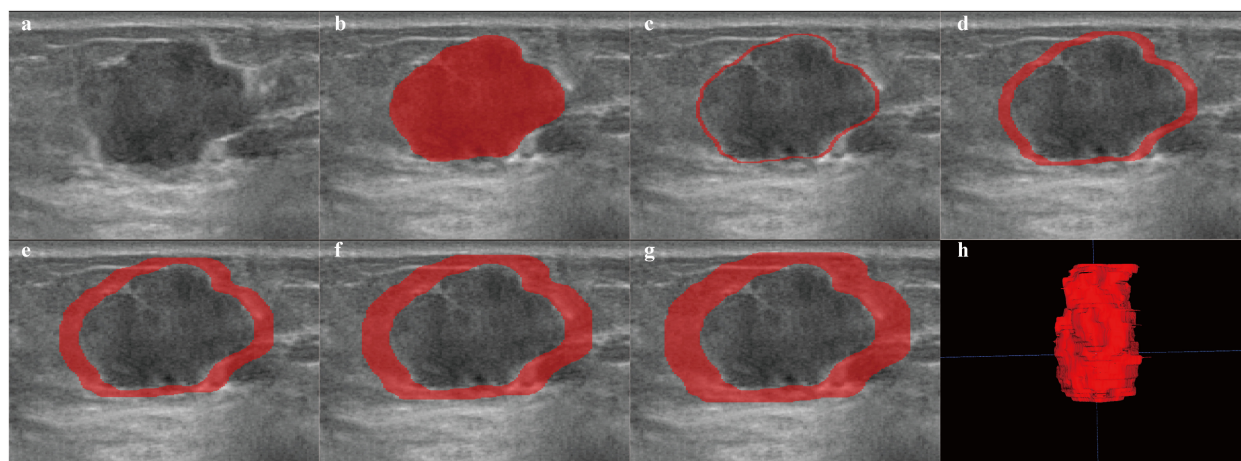
FIGURE 2
Examples of ROI segmentation on ABVS. The red area represents the ROI of the lesion. **(a)** image of the lesion. **(b−g)** ROIs for regions of 1 mm, 3 mm, 5 mm, 7 mm, and 9 mm around the tumor, respectively. **(h)** 3D image of the intratumoral region of the lesion.

calculated for each patient. Methods of preprocessing and ML classifiers are shown in the Appendix A.3.

Radiomics habitat analysis

The k-means method performed cluster analysis on subregions using all data without splitting into training and testing sets. The optimal number of clusters was determined by the elbow method after plotting the within-cluster sum of squares (WCSS) with k values (25). The number of clusters from 1 to 10 was tested in this study. The ITR and PTRs were divided into subregions (habitats) based on optimal k values. Extraction of valuable radiomics features in each habitat and analysis of these features in relation to ER, PR, HER-2, and Ki-67 were conducted.

Construction of Model 2 and Model 3

For sonographic feature variables, univariate logistic regression was used to evaluate their correlation with lymph node metastasis, and factors with $P<0.1$ were introduced into multivariate logistic regression. Factors with $P<0.05$ were identified as independent predictors, whereby an ultrasound feature model was created and named Model 2. RS was combined with ultrasound features to create a sonography radiomics model named Model 3. The Nomo-score was determined for each patient according to Model 2 and Model 3.

Assessment of the models and construction of the nomogram

The predictive performance of Model 1, Model 2, and Model 3 was evaluated by area under curve (AUC) of receiver operating characteristic (ROC), accuracy, sensitivity, and specificity. Plotting Decision Curve Analysis (DCA) assesses the net benefits of the model. Finally, nomogram-model 2 and nomogram-model 3 were constructed based on Model 2 and Model 3.

Associations between Nomo-scores and ALN burden were assessed using correlation analysis. Furthermore, the value of the model for ALN ≥ 3 was assessed based on the Nomo-score cutoff value. (Statistical analyses, Appendix A.4.)

Results

Patient characteristics

The 174 patients enrolled in this study were randomized into a training set (n=121) and a test set (n=53) at a ratio of 7:3. Table 1 displays the distribution of the patients, and no significant difference in training and test sets.

Feature selection, classifiers performance comparison and Model 1 construction

A total of 1688 features were extracted from the ITR and models were constructed using LR, SVM and RF classifiers. The AUC of the LR classifier is highest in the training (0.718) and test (0.725) sets. Appendix A.5 and Appendix Table 1 provide the data preprocessing procedure, three classifier structures and performance.

Extracted features of PTR_{1mm}, PTR_{3mm}, PTR_{5mm}, PTR_{7mm} and PTR_{9mm} PTR. The ITR is modeled in conjunction with the PTR using the LR classifier. ITR+PTR5mm model had AUCs of 0.761 and 0.753 in the training and test sets, respectively, and showed balanced sensitivity, specificity, and accuracy. It was used as the final radiomics model, named Model 1. Based on this model, RS was calculated for each patient. The feature screening and building

TABLE 1 The distribution of the patients.

Variables		Training set	Test set	P
Age (y)		51.9 ± 12.02	53.87 ± 11.77	0.319
ALN	ALN-	78 (64.5%)	38 (71.7%)	0.351
	ALN+	43 (35.5%)	15 (28.3%)	
Histological type	Invasive ductal carcinoma	96 (79.3%)	38 (71.7%)	0.508
	Invasive lobular carcinoma	8 (6.6%)	4 (7.5%)	
	Others	17 (14%)	11 (20.8%)	
Estrogen receptor	Negative	30 (24.8%)	15 (28.3%)	0.627
	Positive	91 (75.2%)	38 (71.7%)	
Progesterone receptor	Negative	28 (23.1%)	10 (18.9%)	0.53
	Positive	93 (76.9%)	43 (81.1%)	
HER-2	Negative	70 (57.9%)	34 (64.2%)	0.652
	Positive	26 (21.5%)	11 (20.8%)	
	Missing	25 (20.7%)	8 (15.1%)	
Ki-67	Negative (<14%)	26 (21.5%)	15 (28.3%)	0.33
	Positive (>14%)	95 (78.5%)	38 (71.7%)	
Lesion maximum diameter (mm)		22.26 ± 8.17	21.76 ± 10.06	0.731
Distance from nipple (mm)		41.26 ± 21.24	40.02 ± 20.26	0.719
Distance from skin (mm)		6.78 ± 2.9	7.35 ± 3.78	0.283
Tumor location	Left	66 (54.5%)	29 (54.7%)	0.983
	Right	55 (45.5%)	24 (45.3%)	
Quadrant	Upper inner	33 (27.3%)	6 (11.3%)	0.109*
	Lower inner	13 (10.7%)	8 (15.1%)	
	Upper outer	47 (38.8%)	22 (41.5%)	
	Lower outer	27 (22.3%)	15 (28.3%)	
	Central	1 (0.8%)	2 (3.8%)	
Shape	Regular	19 (15.7%)	7 (13.2%)	0.671
	Irregular	102 (84.3%)	46 (86.8%)	
Margin	Circumscribed	12 (9.9%)	7 (13.2%)	0.522
	Non-circumscribed	109 (90.1%)	46 (86.8%)	
Orientation	Parallel	95 (78.5%)	42 (79.2%)	0.913
	Non-parallel	26 (21.5%)	11 (20.8%)	
Microcalcification	Without	80 (66.1%)	36 (67.9%)	0.816
	With	41 (33.9%)	17 (32.1%)	
Echogenicity	Hypo-echoic	105 (86.8%)	48 (90.6%)	0.176
	hybrid echo	3 (2.5%)	3 (5.7%)	
	Extremely low echo	13 (10.7%)	2 (3.8%)	
Convergence sign	No	42 (34.7%)	18 (34%)	0.924
	Yes	79 (65.3%)	35 (66%)	

ALN, axillary lymph node; HER-2, human epidermal growth factor receptor 2 *The likelihood ratio test is used.

TABLE 2   The performance of the radiomics model for the intratumor and peritumor combinations.

	Train				Test			
	AUC (95%CI)	ACC	SEN	SPE	AUC (95%CI)	ACC	SEN	SPE
ITR	0.718 (0.626-0.81)	0.661	**0.814**	0.577	0.725 (0.56-0.889)	0.774	**0.733**	0.789
ITR+ PTR$_{1mm}$	0.734 (0.639-0.829)	0.669	0.744	0.628	**0.774 (0.611-0.936)**	**0.811**	0.667	**0.868**
ITR+ PTR$_{3mm}$	0.725 (0.627-0.824)	**0.760**	0.442	**0.936**	0.732 (0.569-0.894)	0.774	0.667	0.816
ITR+ PTR$_{5mm}$	**0.761 (0.673-0.85)**	0.702	0.767	0.667	0.753 (0.584-0.921)	0.792	**0.733**	0.816
ITR+ PTR$_{7mm}$	0.732 (0.636-0.828)	0.694	0.721	0.679	0.718 (0.555-0.88)	0.736	0.600	0.789
ITR+ PTR$_{9mm}$	0.735 (0.64-0.83)	0.702	0.721	0.692	0.712 (0.55-0.875)	0.736	0.600	0.789

Bold characters in the table indicate the best performance for each metric in this study. ITR, intratumoral region; PTR, peritumoral region; ACC, accuracy; SEN sensitivity; SPE, specificity.

methods are described in Appendix A.6 and Appendix Table 2. The performance of the radiomics models for the ITR and PTR combinations are shown in Table 2.

Radiomics habitat analysis

Following the k-means clustering method, ITR and PTR$_{5mm}$ were classified into three habitats (Appendix Figure 2, Figure 3). Detailed steps for the habitat analysis are given in Appendix A.7. The results show that the exponential_ngtdm_Busyness of PTR$_{5mm}$ Habitat-2 differed in PR expression (P=0.034) and Exponential_ngtdm_Busyness of PTR$_{5mm}$ Habitat-3 differed differs in HER-2 expression (P=0.004). Habitat radiomics features with the distribution of ER, PR, HER-2, and Ki-67 expression are shown in the Appendix Table 3.

Model 2 and Model 3 establishment

Multivariate regression in the training set showed that diameter and microcalcification were independent predictors of ALN+ (Table 3). These factors were used to construct Model 2. After adding RS features to the model, RS and microcalcification were independent predictors of ALN+, and these factors were used to construct Model 3. The Nomo-score of the patients was calculated as follows:

Nomo-score (Model 2) =-2.904 + 1.445* Microcalcification
   + 0.077*Diameter
Nomo-score (Model 3) =-0.521 + 1.063*RS
   +1.518*Microcalcification

The performance of Model 1, Model 2, and Model 3 are shown in Table 4. In the training set, model 3 outperforms model 1 and model 2 (Delong test, P=0.033 and 0.027, respectively). AUC of Model 3 was also higher than that of the other 2 models in the test set. The ROC curves of the three models are shown in Figures 4a, b.

The DCA curve also reveals that Model 3 had the highest net benefit in most of the threshold probabilities (Figures 4c, d).

Assessment of the models and construction of the nomogram

Nomogram-model 2 and nomogram-model 3 were constructed based on the factors of Model 2 and Model 3, respectively (Figures 5a, b). The calibration curves and nonsignificant Hosmer-Lemeshow test statistics (0.894 and 0.568 for the nomogram-model 2 training and test sets, respectively, and 0.538 and 0.148 for the nomogram-model 3 training and test sets, respectively) show that the training and test sets are well calibrated, suggesting that the nomogram can show good agreement between predictions and observations (Figures 5c–f).

As shown in Figure 6a, the Nomo-score (Model 2) was positively correlated with the ALN burden (training set r=0.375, P<0.001; test set r=0.410, P=0.002). The optimal threshold when using the Nomo-score to predict ALN state was 47.778 (Youden=0.357). When the Nomo-score was ≥47.778, 54.6% (6/11, training set) and 100% (3/3, test set) of patients had at least 3 ALNs.

As shown in Figure 6b, the Nomo-score (Model 3) was also positively correlated with the ALN burden (training set r=0.552, P<0.001; test set r=0.473, P<0.000). The optimal threshold when using the Nomo-score to predict ALN state was 60.237 (Youden=0.616). When the Nomo-score was ≥60.237, 81.8% (9/11, training set) and 100% (3/3, test set) of patients had at least 3 ALNs.

Discussion

In this study, we developed nomogram-model 2 and nomogram-model 3 capable of effectively assessing ALN metastasis in AUS-negative early breast cancer with AUC,

TABLE 3 Univariate and multivariate logistic regression analysis of variables associated with ALN+.

	Univariate		Multivariate Model 2		Multivariate Model 3	
	OR (95%CI)	P	OR (95%CI)	P	OR (95%CI)	P
Age	1.012 (0.981-1.044)	0.445	–	–	–	–
Lesion maximum diameter(mm)	1.073 (1.022-1.127)	0.005	1.08 (1.026-1.138)	0.004	–	0.769
Distance from nipple (mm)	0.993 (0.975-1.011)	0.429	–	–	–	–
Distance from skin (mm)	0.989 (0.869-1.126)	0.872	–	–	–	–
Tumor location (Ref. center)	0.798(0.376-1.691)	0.556	–	–	–	–
Quadrant						
Upper inner	Ref.	0.998	–	–	–	–
Lower inner	1.094 (0.291-4.109)	0.894	–	–	–	–
Upper outer	0.903 (0.356-2.292)	0.830	–	–	–	–
Lower outer	1.029 (0.358-2.957)	0.957	–	–	–	–
Central	0	1.000	–	–	–	–
Shape (Ref.Regular)	1.662 (0.555-4.98)	0.364	–	–	–	–
Margin (Ref.Circumscribed)	0.749 (0.223-2.521)	0.641	–	–	–	–
Orientation (Ref.Parallel)	0.95 (0.382-2.361)	0.912	–	–	–	–
Microcalcification (Ref.without)	3.833 (1.726-8.513)	0.001	4.242 (1.825-9.858)	0.001	4.563 (1.816-11.463)	0.001
echogenicity						
Hypo-echoic	Ref.	0.541	–	–	–	–
hybrid echo	3.833 (0.336-43.719)	0.279	–	–	–	–
Extremely low echo	1.198 (0.365-3.929)	0.766	–	–	–	–
convergence sign (Ref.no)	0.988 (0.452-2.159)	0.976	–	–	–	–
RS	2.718 (1.719-4.299)	0.000	–	–	2.896 (1.763-4.758)	<0.001

Ref, reference; RS, radiomics-score; OR, Odds ratio;CI, confidence interval.

accuracy, sensitivity, and specificity of 0.708, 0.717,0.733, 0.711; 0.768, 0.755, 0.733, 0.763, respectively. This method was effective in reducing unnecessary SLNB. Both nomograms are also effective in assessing axillary lymph node burden, and it helps clinics make effective treatment decisions, thereby reducing over- or under-treatment. In addition, habitat analysis showed that the radiomics features of the PTR_{5mm} subregion differed in the expression of PR and HER-2, which provided a basis for the validity of the model.

Axillary staging, in addition to biological and anatomical staging of the tumor, is very important in the treatment and prognosis of breast cancer. AUS is the most effective radiologic method for evaluating ALNs (8–10). Ultrasound reporting of suspicious LNs has been shown in several studies to have a significant influence in predicting ALN+ (12, 13, 26), but ultrasound has a high false-negative rate of predicting ALNs (15.5%-35.0%) (11–13). To maximize the performance of ultrasound in predicting ALNs, we focused on ultrasound-negative ALNs.

In the construction of Model 1, we differ from other models that only analyze the radiomics features within the tumor (12); we combined ITR and PTR features and obtained the best imaging

histology model in the $ITR+PTR_{5mm}$ model. Three radiomics features were screened, one from the ITR (wavelet.LLL_glcm_Imc2) and two from the PTR (exponential_ngtdm_Busyness,

TABLE 4 Performance of Model 1, Model 2 and Model 3 in the training and test sets.

	AUC (95%CI)	ACC	SEN	SPE	P values
Training					
Model 1	0.761 (0.673-0.85)	0.702	0.767	0.667	0.033
Model 2	0.742 (0.653-0.831)	0.653	0.767	0.59	0.027
Model 3	0.827 (0.748-0.906)	0.793	0.86	0.756	Ref.
Test					
Model 1	0.753 (0.584-0.921)	0.792	0.733	0.816	0.719
Model 2	0.708 (0.534-0.881)	0.717	0.733	0.711	0.352
Model 3	0.768 (0.61-0.927)	0.755	0.733	0.763	Ref.

Ref, reference; P values were derived from the DeLong test; CI, confidence interval; ACC, accuracy; SEN, sensitivity; SPE, specificity.
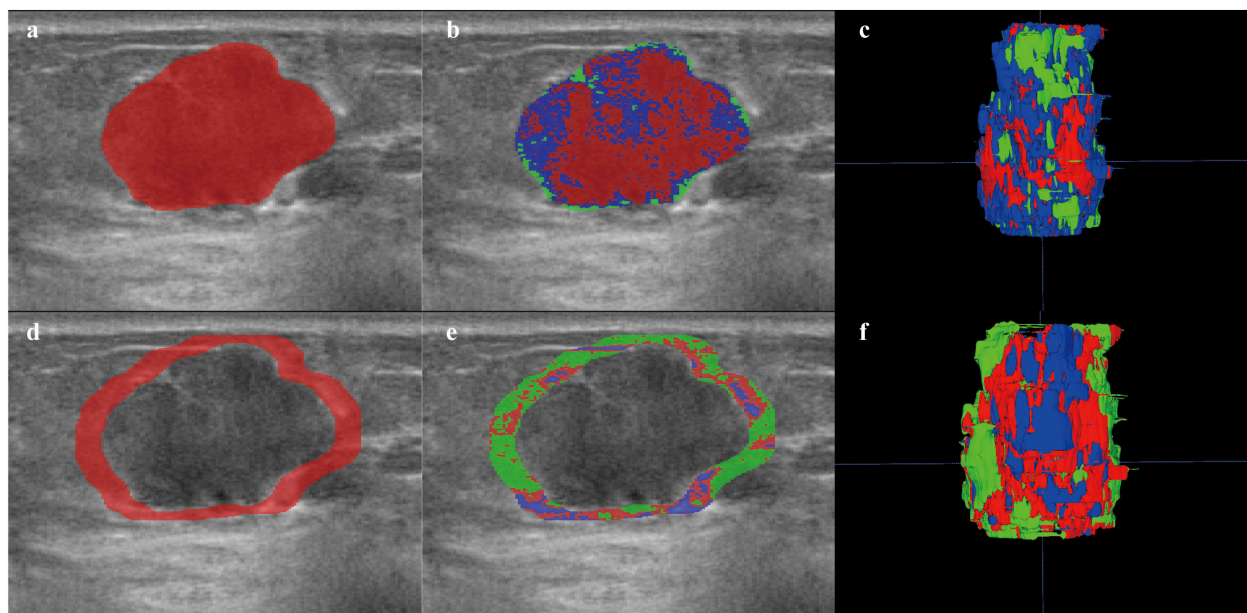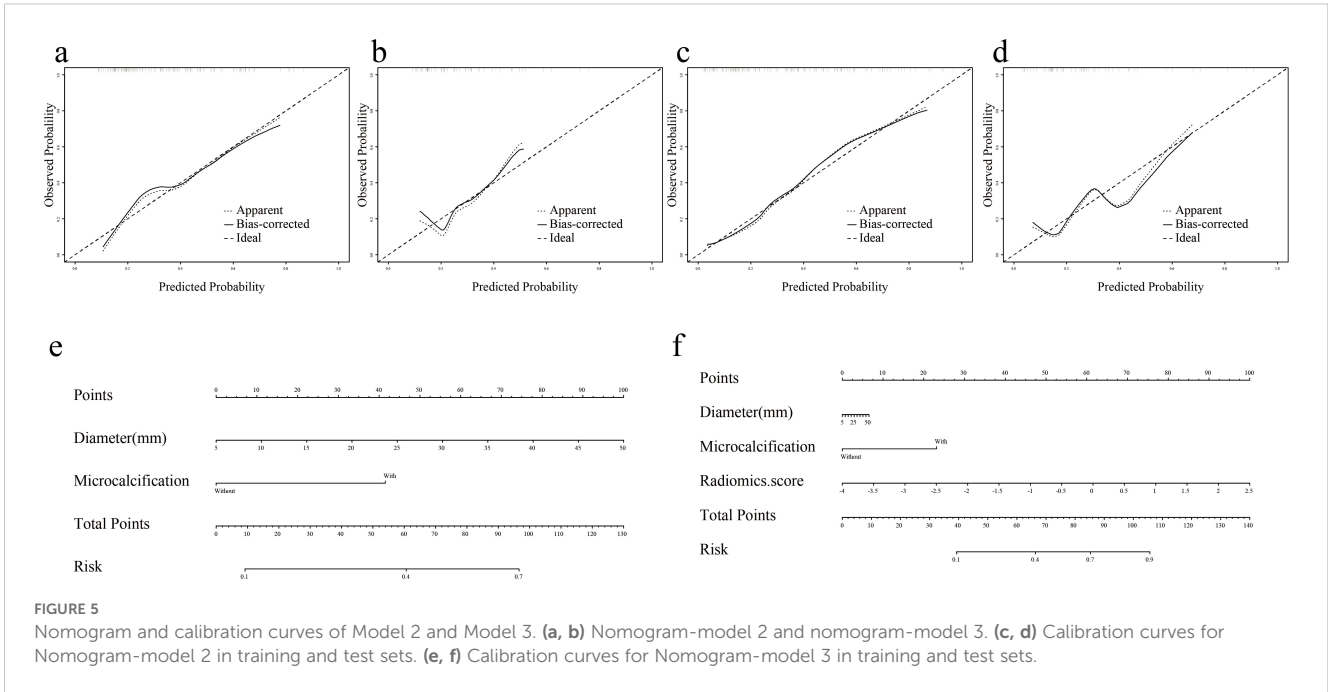
FIGURE 3
Habitat image of breast lesions ITR and PTR$_{5mm}$. **(a)** ROI of ITR. **(b)** habitat image of the ITR. **(c)** three-dimensional imaging of ITR habitat image.
(d) ROI of PTR$_{5mm}$. **(e)** habitat image of the PTR$_{5mm}$. **(f)** three-dimensional imaging of the PTR$_{5mm}$ habitat image. Red, green, and blue represent
Habitat-1, Habitat-2, and Habitat-3, respectively. ITR, intratumoral region; PTR, peritumoral region.
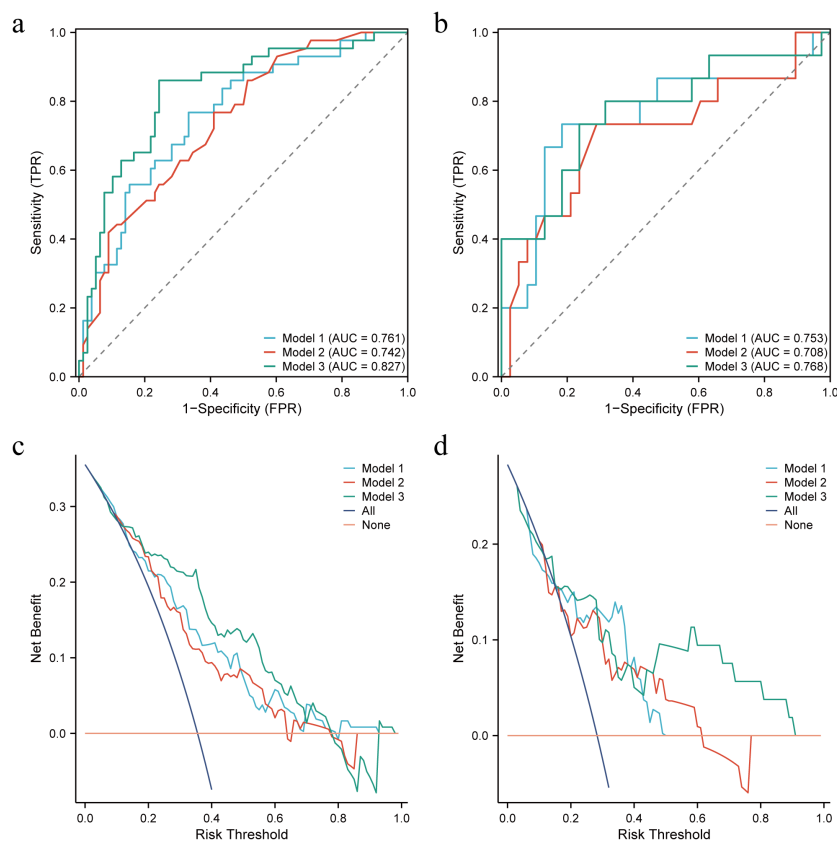
FIGURE 4
Receiver operating characteristic (ROC) curves and decision curves (DCA) for the three models in the training and test sets. **(a, b)** ROC for the
training and test sets of the three models, respectively. **(c, d)** DCA for the training and test sets of the three models, respectively.
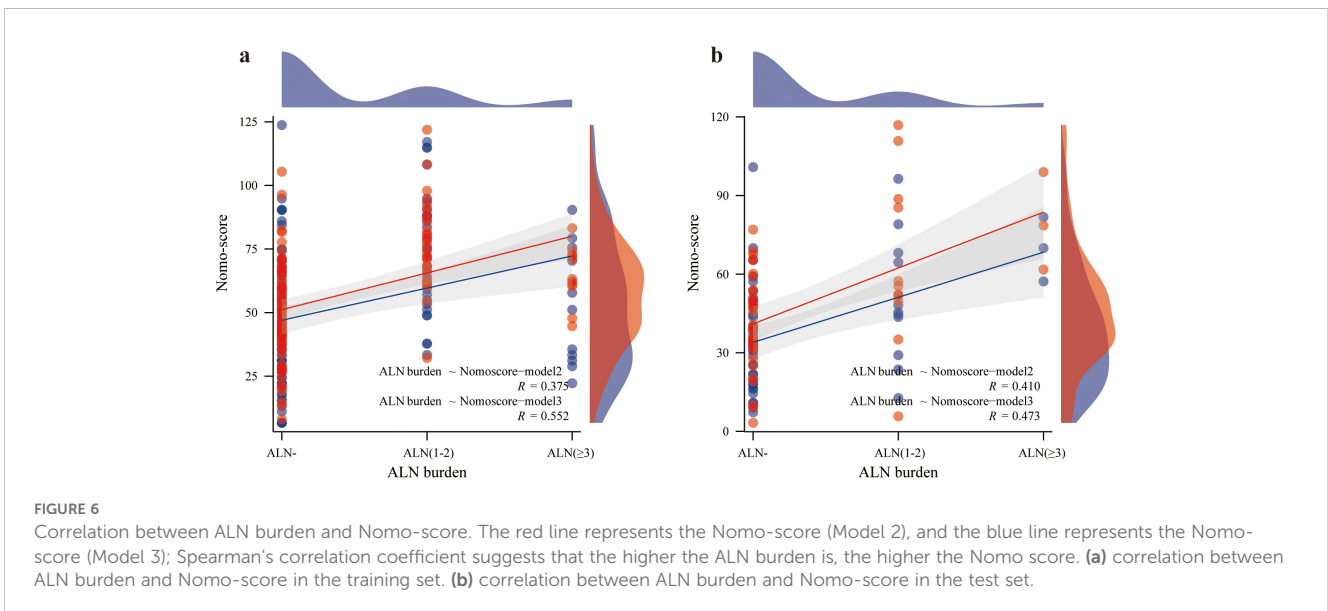
FIGURE 5

Nomogram and calibration curves of Model 2 and Model 3. **(a, b)** Nomogram-model 2 and nomogram-model 3. **(c, d)** Calibration curves for Nomogram-model 2 in training and test sets. **(e, f)** Calibration curves for Nomogram-model 3 in training and test sets.

wavelet.LHL_glszm_SizeZoneNonUniformityNo- rmalized). This suggests that the PTR improves predictive performance in radiographic analysis (27). This is because the peritumoral environment secretes many growth factors and cytokines that can induce hypoxia and angiogenesis, which play an important role in tumorigenesis, progression, or metastasis. Integrating tumor and peritumor data allows for a more comprehensive characterization of tumor invasion and metastasis (28).

The complex vascular system within a tumor result in intratumoral heterogeneity. Heterogeneity is uniformly scattered across the tumor, and regional phenotypic variation inside the tumor is then overlooked (29). Based on speculation by some scholars, the subregions containing voxels with similar imaging characteristics will share common tumor biology properties (30, 31). Habitat analysis methods were developed to divide tumors into subregions containing clusters of voxels with similar characteristics, which allows for better quantification of heterogeneity within the tumor (32, 33). Recently the method has made significant breakthroughs in the assessment of lung, colorectal, and ovarian cancers (34, 35). In this study, an unsupervised clustering method was used to classify the ITR and the PTR$_{5mm}$ area of breast tumors into three categories. The results showed that the distribution of the exponential_ngtdm_Busyness feature of Habitat-2 and the exponential_ngtdm_Busyness feature of Habitat-3 in the PTR$_{5mm}$ was correlated with the expression of PR and HER-2, and it has been demonstrated that patients with different expression of PR and HER-2

FIGURE 6

Correlation between ALN burden and Nomo-score. The red line represents the Nomo-score (Model 2), and the blue line represents the Nomo-score (Model 3); Spearman's correlation coefficient suggests that the higher the ALN burden is, the higher the Nomo score. **(a)** correlation between ALN burden and Nomo-score in the training set. **(b)** correlation between ALN burden and Nomo-score in the test set.

tended to have differences in ALN status (12, 36, 37). This provides strong evidential support for our model and further demonstrates the reliability of the model in predicting ALN status in breast tumors.

Ultrasound characteristics of the tumor are also valuable in the diagnosis of ALN metastases. In a recent report, Xiong et al. (18) combined sonographic features and clinicopathologic features for the prediction of AUS-negative ALNs, with AUCs of 0.705 and 0.745 for the training and test sets, respectively, and showed results similar to those of model 2 in this study. However, pathology indicators were not included in our nomogram, and some histopathology can only be assessed after surgical resection or after aspiration, which may limit the use of the model. Furthermore, in our study, microcalcification was an important factor in the diagnosis of ALN+ (13). Calcification of the tumor is often indicative of a poor prognosis (38), and calcium deposits in the necrotic areas of the tumor appear as gravel or pinpoints, occurring mainly in clusters. Xiong et al. (18) did not analyze calcification, probably because ultrasound does not preserve all images of the lesion, making it difficult to perform an accurate analysis in a retrospective study of the presence or absence of calcification in the lesion. With ABVS, in addition to preserving the complete breast image for subsequent analysis, it also shows microcalcifications more clearly than conventional ultrasound (39). Irregularly shaped ultrasound features in breast cancer significantly correlate with ALN metastasis (40). In invasive breast cancer, cancer cells may infiltrate the surrounding tissue at varying growth rates, creating inconsistent tumor margins. The margins may produce irregular shapes, whereas margins presenting as fuzzy, microfollicular, or acinar may not directly form irregular shapes (13). In our study, however, there was no significant difference in AUS-negative lesions, but the availability of peripheral regions in radiomics explains this phenomenon. Differences in the margins of AUS-negative tumors have altered textural features, although they cannot be recognized by the naked eye. The diameter of the lesion is a major predictor of ALN as well (13, 15–17). Larger breast cancers have more extensive glandular invasion by cancer cells and a higher likelihood of metastatic ALNs via lymphatic drainage (41). The results of Model 2 also showed that tumor diameter was an important predictor of ALN metastasis, which is consistent with previous reports. In patients with invasive breast cancer, there is a nonlinear association between tumor size and ALN metastasis (13, 16), which further emphasizes the important role of tumor diameter in predicting ALN metastasis. Sonogram features are usually combined with radiomics features to further improve diagnostic performance (17, 19, 20). In this study, Model 3 combines the features of Model 1 and Model 2, and it obtained the highest AUC (training set: 0.827, test set: 0.768), and the DCA curve also showed that model 3 had a high net benefit.

Based on the results of the Z0011 trial, the clinical practice guidelines were updated to state that women with T1 or T2 primary invasive breast cancer with 1-2 metastatic SLNs who are scheduled to undergo breast-conserving surgery with whole-breast radiotherapy no longer need ALND (6, 42). Assessing ALN burden is also critical. The

nomogram in this study was able to differentiate between ALN- and ALN+ patients. It also has better results for identifying ALN statuses with a high burden. A positive correlation between the Nomo-score and ALN burden is shown in Figure 6. The higher the Nomo-score is, the greater the likelihood of a high ALN burden. Combined with the optimal thresholds, nomogram-model 2 screens 54.6-100% of those with an ALN high burden. Nomogram-model 3 screens 81.8-100% of those with a high ALN burden. This will increase surgeon confidence in performing ALND based on a positive SLN.

There are some limitations in this study. First, this was a single-center retrospective study. The nongeneralizability of the ABVS examination resulted in a small sample size for this study, and prospective and multicenter studies may be conducted in the future for further validation. Second, influenced by different regional breast cancer management guidelines and subjective patient factors, some HER-2 positive patients in this study did not receive neoadjuvant therapy prior to surgery. In future studies, we will further expand the sample size and include patients receiving neoadjuvant therapy, so as to provide treatment recommendations for more breast cancer patients. Third, the ROI for each lesion was manually defined, and although we removed features with ICCs < 0.75, interobserver variability was unavoidable. In the future, we will solve this by automatic or semiautomatic segmentation. Lastly, owing to the difficulty of accurately drawing ROIs for nonoccupying lesions without borders and the difficulty of identifying which lesion is the cause of metastatic ALN for multiple lesions, these two types of lesions were excluded. This may cause selection bias and nomogram restriction.

In conclusion, two nomograms were developed and validated in this study: one based on sonogram features named nomograms-Model 2; and one based on sonogram and radiomics features named nomograms-Model 3. They can predict ALN status more accurately in AUS-negative breast cancer patients and also show good performance in assessing ALN burden. These two nomograms can effectively help clinicians in the preoperative assessment of ALN status and contribute to the optimization of clinical decision-making in breast cancer patients.

Data availability statement

The raw data supporting the conclusions of this article will be made available by the authors, without undue reservation.

Ethics statement

The studies involving humans were approved by Ethics Committee of Anhui Medical University (PJ2023-07-11). The studies were conducted in accordance with the local legislation and institutional requirements. The ethics committee/institutional review board waived the requirement of written informed consent for participation from the participants or the participants' legal guardians/next of kin because we conducted a retrospective analysis

of patient data and the anonymous data used, so we abandoned written informed consent forms to prevent potential bias.

Conflict of interest

The authors declare that the research was conducted in the absence of any commercial or financial relationships that could be construed as a potential conflict of interest.

Publisher's note

All claims expressed in this article are solely those of the authors and do not necessarily represent those of their affiliated organizations, or those of the publisher, the editors and the reviewers. Any product that may be evaluated in this article, or claim that may be made by its manufacturer, is not guaranteed or endorsed by the publisher.

Supplementary material

The Supplementary Material for this article can be found online at: https://www.frontiersin.org/articles/10.3389/fimmu.2025.1460673/full#supplementary-material

References

1. Chang JM, Leung JWT, Moy L, Ha SM, Moon WK. Axillary nodal evaluation in breast cancer: state of the art. *Radiology*. (2020) 295:500–15. doi: 10.1148/radiol.2020192534

2. Ahmed M, Purushotham AD, Douek M. Novel techniques for sentinel lymph node biopsy in breast cancer: a systematic review. *Lancet Oncol*. (2014) 15:e351–62. doi: 10.1016/S1470-2045(13)70590-4

3. Hindie E, Groheux D, Brenot-Rossi I, Rubello D, Moretti JL, Espie M. The sentinel node procedure in breast cancer: nuclear medicine as the starting point. *J Nucl Med*. (2011) 52:405–14. doi: 10.2967/jnumed.110.081711

4. Alsumai TS, Alhazzaa N, Alshamrani A, Assiri S, Alhefdhi A. Factors predicting positive sentinel lymph node biopsy in clinically node-negative breast cancer. *Breast Cancer (Dove Med Press)*. (2022) 14:323–34. doi: 10.2147/BCTT.S373005

5. Lucci A, Mccall LM, Beitsch PD, Whitworth PW, Reintgen DS, Blumencranz PW, et al. Surgical complications associated with sentinel lymph node dissection (SLND) plus axillary lymph node dissection compared with SLND alone in the American College of Surgeons Oncology Group Trial Z0011. *J Clin Oncol*. (2007) 25:3657–63. doi: 10.1200/JCO.2006.07.4062

6. Giuliano AE, Ballman KV, Mccall L, Beitsch PD, Brennan MB, Kelemen PR, et al. Effect of axillary dissection vs no axillary dissection on 10-year overall survival among women with invasive breast cancer and sentinel node metastasis: the ACOSOG Z0011 (Alliance) randomized clinical trial. *JAMA*. (2017) 318:918–26. doi: 10.1001/jama.2017.11470

7. Giuliano AE, Hunt KK, Ballman KV, Beitsch PD, Whitworth PW, Blumencranz PW, et al. Axillary dissection vs no axillary dissection in women with invasive breast cancer and sentinel node metastasis: a randomized clinical trial. *JAMA*. (2011) 305:569–75. doi: 10.1001/jama.2011.90

8. Feng Y, Huang R, He Y, Lu A, Fan Z, Fan T, et al. Efficacy of physical examination, ultrasound, and ultrasound combined with fine-needle aspiration for axilla staging of primary breast cancer. *Breast Cancer Res Treat*. (2015) 149:761–5. doi: 10.1007/s10549-015-3280-z

9. Majid S, Tengrup I, Manjer J. Clinical assessment of axillary lymph nodes and tumor size in breast cancer compared with histopathological examination: a population-based analysis of 2,537 women. *World J Surg*. (2013) 37:67–71. doi: 10.1007/s00268-012-1788-5

10. Cools-Lartigue J, Meterissian S. Accuracy of axillary ultrasound in the diagnosis of nodal metastasis in invasive breast cancer: A review. *World J Surg*. (2012) 36:46–54. doi: 10.1007/s00268-011-1319-9

11. Ozler I, Aydin H, Guler OC, Esen Bostanci I, Sahin Guner B, Karaman N, et al. Can preoperative axillary ultrasound and biopsy of suspicious lymph nodes be an alternative to sentinel lymph node biopsy in clinical node negative early breast cancer? *Int J Clin Pract*. (2021) 75:e14332. doi: 10.1111/ijcp.14332

12. Jiang M, Li CL, Luo XM, Chuan ZR, Chen RX, Tang SC, et al. Radiomics model based on shear-wave elastography in the assessment of axillary lymph node status in early-stage breast cancer. *Eur Radiol*. (2022) 32:2313–25. doi: 10.1007/s00330-021-08330-w

13. Yi CB, Ding ZY, Deng J, Ye XH, Chen L, Zong M, et al. Combining the ultrasound features of primary tumor and axillary lymph nodes can reduce false-negative rate during the prediction of high axillary node burden in BI-RADS category 4 or 5 breast cancer lesions. *Ultrasound Med Biol*. (2020) 46:1941–8. doi: 10.1016/j.ultrasmedbio.2020.04.003

14. Bae MS, Shin SU, Song SE, Ryu HS, Han W, Moon WK. Association between US features of primary tumor and axillary lymph node metastasis in patients with clinical T1-T2N0 breast cancer. *Acta Radiol*. (2018) 59:402–8. doi: 10.1177/0284185117723039

15. Wang Q, Li B, Liu Z, Shang H, Jing H, Shao H, et al. Prediction model of axillary lymph node status using automated breast ultrasound (ABUS) and ki-67 status in early-stage breast cancer. *BMC Cancer*. (2022) 22:929. doi: 10.1186/s12885-022-10034-3

16. Sopik V, Narod SA. The relationship between tumour size, nodal status and distant metastases: on the origins of breast cancer. *Breast Cancer Res Treat*. (2018) 170:647–56. doi: 10.1007/s10549-018-4796-9

17. Gao Y, Luo Y, Zhao C, Xiao M, Ma L, Li W, et al. Nomogram based on radiomics analysis of primary breast cancer ultrasound images: prediction of axillary lymph node tumor burden in patients. *Eur Radiol*. (2021) 31:928–37. doi: 10.1007/s00330-020-07181-1

18. Xiong J, Zuo W, Wu Y, Wang X, Li W, Wang Q, et al. Ultrasonography and clinicopathological features of breast cancer in predicting axillary lymph node metastases. *BMC Cancer*. (2022) 22(1):1–11. doi: 10.1186/s12885-022-10240-z

19. Ma Q, Wang J, Xu D, Zhu C, Qin J, Wu Y, et al. Automatic breast volume scanner and B-ultrasound-based radiomics nomogram for clinician management of BI-RADS 4A lesions. *Acad Radiol.* (2023) 30(8):1628–37. doi: 10.1016/j.acra.2022.11.002

20. Ma Q, Lu X, Qin X, Xu X, Fan M, Duan Y, et al. A sonogram radiomics model for differentiating granulomatous lobular mastitis from invasive breast cancer: a multicenter study. *Radiol Med.* (2023) 128(10):11. doi: 10.1007/s11547-023-01694-7

21. Brattain LJ, Telfer BA, Dhyani M, Grajo JR, Samir AE. Machine learning for medical ultrasound: status, methods, and future opportunities. *Abdom Radiol (NY).* (2018) 43:786–99. doi: 10.1007/s00261-018-1517-0

22. Guldogan N, Yilmaz E, Arslan A, Kucukkaya F, Atila N, Aribal E. Comparison of 3D-automated breast ultrasound with handheld breast ultrasound regarding detection and BI-RADS characterization of lesions in dense breasts: A study of 592 cases. *Acad Radiol.* (2022) 29:1143–8. doi: 10.1016/j.acra.2021.11.022

23. Lambin P, Leijenaar RTH, Deist TM, Peerlings J, De Jong EEC, Van Timmeren J, et al. Radiomics: the bridge between medical imaging and personalized medicine. *Nat Rev Clin Oncol.* (2017) 14:749–62. doi: 10.1038/nrclinonc.2017.141

24. Lee B, Lim AK, Krell J, Satchithananda K, Coombes RC, Lewis JS, et al. The efficacy of axillary ultrasound in the detection of nodal metastasis in breast cancer. *AJR Am J Roentgenol.* (2013) 200:W314–20. doi: 10.2214/AJR.12.9032

25. Lee H, Choi Y, Son B, Lim J, Lee S, Kang JW, et al. Deep autoencoder-powered pattern identification of sleep disturbance using multi-site cross-sectional survey data. *Front Med (Lausanne).* (2022) 9:950327. doi: 10.3389/fmed.2022.950327

26. Kim SM, Jang M, Yun BL, Shin SU, Rim J, Kang E, et al. Automated versus handheld breast ultrasound for evaluating axillary lymph nodes in patients with breast cancer. *Korean J Radiol.* (2024) 25(2):11. doi: 10.3348/kjr.2023.0100

27. Ding J, Chen S, Serrano Sosa M, Cattell R, Lei L, Sun J, et al. Optimizing the peritumoral region size in radiomics analysis for sentinel lymph node status prediction in breast cancer. *Acad Radiol.* (2022) 29 Suppl 1:S223–8. doi: 10.1016/j.acra.2020.10.015

28. Han X, Cao W, Wu L, Liang C. Radiomics assessment of the tumor immune microenvironment to predict outcomes in breast cancer. *Front Immunol.* (2021) 12:773581. doi: 10.3389/fimmu.2021.773581

29. Gatenby RA, Grove O, Gillies RJ. Quantitative imaging in cancer evolution and ecology. *Radiology.* (2013) 269:8–15. doi: 10.1148/radiol.13122697

30. O'connor JP, Rose CJ, Waterton JC, Carano RA, Parker GJ, Jackson A. Imaging intratumor heterogeneity: role in therapy response, resistance, and clinical outcome. *Clin Cancer Res.* (2015) 21:249–57. doi: 10.1158/1078-0432.CCR-14-0990

31. Dextraze K, Saha A, Kim D, Narang S, Lehrer M, Rao A, et al. Spatial habitats from multiparametric MR imaging are associated with signaling pathway activities and survival in glioblastoma. *Oncotarget.* (2017) 8:112992–3001. doi: 10.18632/oncotarget.22947

32. Liu HF, Wang M, Lu YJ, Wang Q, Lu Y, Xing F, et al. CEMRI-based quantification of intratumoral heterogeneity for predicting aggressive characteristics of hepatocellular carcinoma using habitat analysis: comparison and combination of deep learning. *Acad Radiol.* (2024) 31(6):2346–55. doi: 10.1016/j.acra.2023.11.024

33. Kim J, Ryu SY, Lee SH, Lee HY, Park H. Clustering approach to identify intratumour heterogeneity combining FDG PET and diffusion-weighted MRI in lung adenocarcinoma. *Eur Radiol.* (2019) 29:468–75. doi: 10.1007/s00330-018-5590-0

34. Caii W, Wu X, Guo K, Chen Y, Shi Y, Chen J. Integration of deep learning and habitat radiomics for predicting the response to immunotherapy in NSCLC patients. *Cancer Immunol Immunother.* (2024) 73:153. doi: 10.1007/s00262-024-03724-3

35. Huang H, Chen H, Zheng D, Chen C, Wang Y, Xu L, et al. Habitat-based radiomics analysis for evaluating immediate response in colorectal cancer lung metastases treated by radiofrequency ablation. *Cancer Imaging.* (2024) 24:44. doi: 10.1186/s40644-024-00692-w

36. Van Calster B, Vanden Bempt I, Drijkoningen M, Pochet N, Cheng J, Van Huffel S, et al. Axillary lymph node status of operable breast cancers by combined steroid receptor and HER-2 status: triple positive tumours are more likely lymph node positive. *Breast Cancer Res Treat.* (2009) 113:181–7. doi: 10.1007/s10549-008-9914-7

37. Wang Z, Zhang H, Lin F, Zhang R, Ma H, Shi Y, et al. Intra- and peritumoral radiomics of contrast-enhanced mammography predicts axillary lymph node metastasis in patients with breast cancer: A multicenter study. *Acad Radiol.* (2023) 30:(Suppl 2):S133–S142. doi: 10.1016/j.acra.2023.02.005

38. Yu X, Hao X, Wan J, Wang Y, Yu L, Liu B. Correlation between ultrasound appearance of small breast cancer and axillary lymph node metastasis. *Ultrasound Med Biol.* (2018) 44:342–9. doi: 10.1016/J.ultrasmedbio.2017.09.020

39. Xiao YM, Chen ZH, Zhou QC, Wang Z. The efficacy of automated breast volume scanning over conventional ultrasonography among patients with breast lesions. *Int J Gynaecol Obstet.* (2015) 131:293–6. doi: 10.1016/j.ijgo.2015.05.036

40. Guo Q, Dong Z, Zhang L, Ning C, Li Z, Wang D, et al. Ultrasound features of breast cancer for predicting axillary lymph node metastasis. *J Ultrasound Med.* (2018) 37:1354–3. doi: 10.1002/jum.14469

41. Chen Y, Xie Y, Li B, Shao H, Na Z, Wang Q, et al. Automated Breast Ultrasound (ABUS)-based radiomics nomogram: an individualized tool for predicting axillary lymph node tumor burden in patients with early breast cancer. *BMC Cancer.* (2023) 23:340. doi: 10.1186/s12885-023-10743-3

42. Lyman GH, Somerfield MR, Bosserman LD, Perkins CL, Weaver DL, Giuliano AE. Sentinel lymph node biopsy for patients with early-stage breast cancer: american society of clinical oncology clinical practice guideline update. *J Clin Oncol.* (2017) 35:561–4. doi: 10.1200/JCO.2016.71.0947